Time-domain and spectral properties of pulsars at 154 MHz

M. E. Bell,[1,2]⋆ Tara Murphy,[2,3] S. Johnston,[1] D. L. Kaplan,[4] S. Croft,[5,6]
P. Hancock,[2,7] J. R. Callingham,[1,2,3] A. Zic,[3] D. Dobie,[3] J. K. Swiggum,[4]
A. Rowlinson,[8,9] N. Hurley-Walker,[7] A. R. Offringa,[9] G. Bernardi,[10,11,12]
J. D. Bowman,[13] F. Briggs,[14] R. J. Cappallo,[15] A. A. Deshpande,[16]
B. M. Gaensler,[2,3,17] L. J. Greenhill,[12] B. J. Hazelton,[18] M. Johnston-Hollitt,[19]
C. J. Lonsdale,[15] S. R. McWhirter,[15] D. A. Mitchell,[1,2] M. F. Morales,[18] E. Morgan,[5]
D. Oberoi,[19] S. M. Ord,[2,7] T. Prabu,[16] N. Udaya Shankar,[16] K. S. Srivani,[16]
R. Subrahmanyan,[2,16] S. J. Tingay,[2,7] R. B. Wayth,[2,7] R. L. Webster,[2,20]
A. Williams[7] and C. L. Williams[15]

[1]*CSIRO Astronomy and Space Science, PO Box 76, Epping, NSW 1710, Australia*
[2]*ARC Centre of Excellence for All-sky Astrophysics (CAASTRO)*
[3]*Sydney Institute for Astronomy (SIfA), School of Physics, The University of Sydney, NSW 2006, Australia*
[4]*Department of Physics, University of Wisconsin–Milwaukee, 1900 E. Kenwood Boulevard, Milwaukee, WI 53211, USA*
[5]*Astronomy Department, University of California, Berkeley, 501 Campbell Hall #3411, Berkeley, CA 94720, USA*
[6]*Eureka Scientific, Inc., 2452 Delmer Street Suite 100, Oakland, CA 94602, USA*
[7]*International Centre for Radio Astronomy Research, Curtin University, Bentley, WA 6845, Australia*
[8]*Anton Pannekoek Institute, University of Amsterdam, Postbus 94249, NL-1090 GE Amsterdam, the Netherlands*
[9]*Netherlands Institute for Radio Astronomy (ASTRON), PO Box 2, NL-7990 AA Dwingeloo, the Netherlands*
[10]*SKA SA, 3rd Floor, The Park, Park Road, Pinelands 7405, South Africa*
[11]*Department of Physics and Electronics, Rhodes University, PO Box 94, Grahamstown 6140, South Africa*
[12]*Harvard–Smithsonian Center for Astrophysics, Cambridge, MA 02138, USA*
[13]*School of Earth and Space Exploration, Arizona State University, Tempe, AZ 85287, USA*
[14]*Research School of Astronomy and Astrophysics, Australian National University, Canberra, ACT 2611, Australia*
[15]*MIT Haystack Observatory, Westford, MA 01886, USA*
[16]*Raman Research Institute, Bangalore 560080, India*
[17]*Dunlap Institute for Astronomy and Astrophysics, University of Toronto, ON M5S 3H4, Canada*
[18]*Department of Physics, University of Washington, Seattle, WA 98195, USA*
[19]*School of Chemical and Physical Sciences, Victoria University of Wellington, PO Box 600, Wellington 6140, New Zealand*
[20]*National Centre for Radio Astrophysics, Tata Institute for Fundamental Research, Pune 411007, India*
[21]*School of Physics, The University of Melbourne, Parkville, VIC 3010, Australia*

ABSTRACT

We present 154 MHz Murchison Widefield Array imaging observations and variability information for a sample of pulsars. Over the declination range $-80° < \delta < 10°$, we detect 17 known pulsars with mean flux density greater than 0.3 Jy. We explore the variability properties of this sample on time-scales of minutes to years. For three of these pulsars, PSR J0953+0755, PSR J0437−4715, and PSR J0630−2834, we observe interstellar scintillation and variability on time-scales of greater than 2 min. One further pulsar, PSR J0034−0721, showed significant variability, the physical origins of which are difficult to determine. The dynamic spectra for PSR J0953+0755 and PSR J0437−4715 show discrete time and frequency structure consistent with diffractive interstellar scintillation and we present the scintillation bandwidth and time-scales from these observations. The remaining pulsars within our sample were statistically non-variable. We also explore the spectral properties of this sample and find spectral curvature in pulsars PSR J0835−4510, PSR J1752−2806, and PSR J0437−4715.

Key words: pulsars: general – radio continuum: stars.

⋆ E-mail: martin.bell@csiro.au

1 INTRODUCTION

The time-varying low-frequency radio sky offers a rich parameter space for exploration. With the advent of low-frequency, wide-field, and high-resolution interferometers e.g. the Murchison Wide-field Array (MWA; Lonsdale et al. 2009; Tingay et al. 2013), the Low-Frequency Array (van Haarlem et al. 2013), and the Long Wavelength Array (LWA; Ellingson et al. 2009), it is now feasible to blindly search vast areas of the sky for transient and variable phenomena. The purpose of such surveys is to explore the physical mechanisms (both intrinsic and extrinsic) driving dynamic behaviour in known and unknown classes of sources.

In this paper, we present time-domain measurements of 17 bright pulsars on cadences of minutes, months, and years. These measurements have been made as part of the Murchison Widefield Array Transients Survey (MWATS). MWATS is a time-domain survey covering the declination range $-80° < δ < +10°$ at 154 MHz. For this survey, high-fidelity wide-field (1000 deg^2) images were obtained with integration times of just 112 s. The science goal of MWATS is to provide a blind low-frequency census of transient and variability activity (Bell et al., in preparation).

Pulsars are compact stellar remnants that emit regular pulses as they spin, with significant intrinsic variability on time-scales shorter than a second. A small sub-set of pulsars are known to emit giant radio pulses (e.g. Johnston et al. 2001; Tsai et al. 2015). Giant pulses are typically broad-band in nature with a low duty cycle when compared with normal pulses (see Lorimer & Kramer 2012; Oronsaye et al. 2015). Some pulsars show intermittency on various time-scales (e.g. Kramer et al. 2006; Hobbs et al. 2016). For example, nulling i.e. the absence of detectable radio emission for one or more pulse periods, could modulate the long-term phase-averaged flux density, if the null rate was large (e.g. see Deich et al. 1986).

However, for most pulsars the average emitted flux density is constant when averaged over suitably long time-scales (minutes or longer). The received flux density can be modulated, though, because of propagation effects such as diffractive and refractive interstellar scintillation (Armstrong, Rickett & Spangler 1995) that affects pulsars due to their compact sizes (10^{-3} μarcsec; Lazio et al. 2004). Diffractive interstellar scintillation is the interference of different paths of a ray, between a source and receiver (Goodman 1997). The different paths arise from small-scale inhomogeneities in the interstellar medium (ISM). Diffractive interstellar scintillation can cause variations on time-scales of tens of minutes but is dependent on, for example, dispersion measure (DM), distance, frequency, and pulsar transverse velocity (see Rickett 1977; Cordes 1986). Refractive interstellar scintillation is caused by large-scale electron density irregularities along the line of sight (Bhat, Gupta & Rao 1999b) and constitutes a slower and less-modulated variation in the pulsar flux density over weeks to months (Sieber 1982).

Depending on the cadence of the observations, we can explore different variability regimes for different pulsars. Exploring these different regimes have typically been done via high-time resolution observations, rather than imaging (e.g. see Stappers et al. 2011; Bhat et al. 2014; Tsai et al. 2015; Kondratiev et al. 2016). Long-term studies have specifically aimed at exploring the effects of the ISM. For example, Gupta, Rickett & Coles (1993) present daily phase-averaged flux densities of nine pulsars over a duration of 400 d. For the majority of pulsars in their sample, the flux density changes were consistent with those predicted by refractive interstellar scintillation (also see Kaspi & Stinebring 1992, Stinebring et al. 2000, and Zhou et al. 2003).

Imaging observations can offer an alternative and convenient way of studying and possibly even discovering pulsars (e.g. Backer et al. 1982; Kaplan et al. 1998). With the increased survey speed of next generation wide-field instruments, much of this information comes for free. In this paper, we present a time-domain survey of a sample of 17 known pulsars. This survey allows us to probe the short- and long-term effects of the ISM on pulsar flux densities at low frequencies, and more generally the variability properties of this sample. In addition, we evaluate the ability for the MWA to study pulsars via imaging observations and its applications to future surveys.

In Section 2 of this paper, we present the observing strategy and pulsar sample selection. In Section 3, we discuss the data-reduction strategy and variability statistics used to characterize the sample. In Section 4, we present the results of our analysis focusing on the pulsars that showed significant variability. In Section 5, we discuss our results and explore what might be achieved with similar but deeper surveys using image plane techniques.

2 OBSERVING STRATEGY AND PULSAR SAMPLE SELECTION

Data collection for this survey began in 2013 July and ended in 2015 July. The observing cadence was approximately one night per month, and on each night we typically observed for 10 h. Observations were conducted at a centre frequency of 154 MHz with an observing bandwidth of 30.72 MHz. A channel bandwidth of 40 KHz and a correlator integration time of either 0.5 or 2 s were used for these observations. The correlator integration time was increased to 2 s in later observations to reduce data rates.

We used a drift scanning strategy to cover a large sky area each night. Utilizing night-time seasonal sky rotation allows for sampling the entire hemisphere over 1 yr. A given pulsar takes approximately one hour to drift through the primary beam (full width at half-maximum of 24°.4 at 154 MHz). The observing strategy was to cycle through three different pointings along the meridian at $δ = -55°, -26°$ (zenith), and $+1.6°$. These declination strips overlap giving complete sky coverage between $+10°$ and $-80°$. A 112 s snapshot observation was obtained at each of these declinations in turn for the duration of the observing run. Due to the observing strategy, for a given declination, a 4 min gap occurs between observations. An additional 8 s are required to update the correlator configuration for a new pointing. A summary of the observing specifications are given in Table 1.

Two data products were generated from this survey: (1) single snapshot images, used to generate the light curves of the pulsars (discussed below); and (2) mosaicked monthly images formed from all snapshots for a given declination. These images were used for the initial identification of the pulsars in our sample.

We used the Australia Telescope National Facility (ATNF) pulsar data base[1] (version 1.54; date accessed 2015-05-01) to determine positions of known pulsars in our survey region. There were 2297 known pulsars in our survey region of declination $<+10°$. We searched for detections at the positions of each pulsar in our monthly mosaicked images. If a detection was made, the statistics were recorded, e.g. signal-to-noise ratio, flux density etc. Of a total 2297 pulsars that were within our sky area over 100 were detected above the $3σ$ noise level. For this analysis, we focused on extracting variability information, so we concentrated on bright, well-detected

[1] http://www.atnf.csiro.au/people/pulsar/psrcat/

Table 1. Properties of observations. Typical noise values are quoted in the extragalactic direction for $b > 10°$ and in the galactic direction for $b < 10°$.

Property	Value
Integration time per snapshot	112 s
Number of snapshots per pulsar	55–159
Cadence	minutes, months, and years
Image size (pixels)	3072×3072
Frequency	154 MHz
Bandwidth	30.72 MHz
Channel bandwidth	40 KHz
Pixel diameter	0.75 arcmin
Resolution at 154 MHz	2.4 arcmin
Briggs weighting	-1
UV range (kλ)	>0.03 kλ
Declinations	$+1°\!.6, -26°, -55°$
Typical image noise (extragalactic pointing)	20 mJy
Typical image noise (galactic pointing)	100 mJy

pulsars that had adequate signal-to-noise ratio ($>8\sigma$) in the monthly mosaicked images. This restricted our final sample of pulsars to 17 (see Table 2 for details). A more complete analysis of all pulsar detections will be presented in future work.

3 DATA REDUCTION

3.1 Phase calibration, flagging, imaging, and self-calibration

Phase calibration was performed as follows. A snapshot observation (with integration time 112 s) of a well-modelled bright source was obtained for phase calibration purposes as a function of declination strip and observing run. Model images of these calibrator sources were extracted from the Sydney University Molonglo Sky Survey (SUMSS; Mauch et al. 2003) or the VLA Low-frequency Sky Survey (VLSS; Cohen et al. 2007). The model image of the calibrator source was inverse-Fourier transformed to generate a set of model visibilities. A single time-independent, frequency-dependent amplitude, and phase calibration solution was derived from this model with respect to the calibrator observation visibilities. These gain solutions were then applied to the appropriate target visibilities (discussed below). We will discuss flux density scale corrections in Section 3.2.

For each of the snapshot target observations, we performed the following processing.

(i) Data were flagged for radio frequency interference using the AOFLAGGER algorithm (Offringa, van de Gronde & Roerdink 2012) and converted into CASA measurement set format using the MWA pre-processing pipeline COTTER. Approximately 1 per cent of the visibilities were removed at this stage, see Offringa et al. (2015) for a thorough discussion.

(ii) Phase and amplitude calibration solutions were applied to the visibilities (as discussed above).

(iii) The visibilities were deconvolved and CLEANed with 2000 iterations using the WSCLEAN algorithm (Offringa et al. 2014). An rms noise measurement was taken from the images to ascertain an appropriate CLEAN threshold for post-self-calibration imaging.

(iv) The CLEAN component model was inverse-Fourier transformed for self-calibration purposes. A new set of phase and amplitude calibration solutions were derived from this model and applied to the data.

(v) The visibilities were then deconvolved and CLEANed to a cut-off of three times the rms derived from the pre-self-calibration image. An image size of 3072×3072 with pixel diameter 0.75 arcmin and robust parameter of -1 was used.

(vi) A primary beam correction was applied to create Stokes I images. See Offringa et al. (2014) for further details.

As discussed above, two different data products were generated from the data reduction. First, we reduced a smaller sub-set of the total data covering approximately one year and all of our survey area. For a given night and declination strip, all snapshot images were mosaicked together. We used these mosaics to construct our initial sample of detected pulsars. Secondly, we reduced all available

Table 2. Variability of pulsars in this sample. Above the horizontal line are the pulsars that showed significant variability sorted by χ_r^2. The pulsars below the line remain non-variable and are sorted by right ascension. The column labelled M indicates the modulation index of the pulsar, the $\overline{M}$ column indicates the average modulation index of two nearby sources. The minimum, maximum, and average flux densities of the pulsars are denoted by S_{min}, S_{max} and $\overline{S}$, respectively. The total number of observations is denoted by N. Pulsars located $>12°$ from the pointing centre of the observations are marked with a dagger (†) symbol.

Pulsar name	B name	DM (cm^{-3} pc)	M (per cent)	S_{min} (Jy)	S_{max} (Jy)	$\overline{S}$ (Jy)	N	χ_r^2	$\overline{M}$ (per cent)
PSR J0953+0755	B0950+08	2.95	131.3	0.27	16.4	2.6 ± 0.8	83	182.1	17.4
PSR J0437−4715	–	2.65	44.9	0.32	2.0	0.87 ± 0.3	55	28.1	7.5
PSR J0630−2834	B0628−28	34.5	30.0	0.33	1.18	0.64 ± 0.2	87	5.8	10.5
PSR J0034−0721†	B0031−07	11.4	45.0	0.24	1.8	0.64 ± 0.2	90	2.0	25.7
PSR J0835−4510	B0833−45	68.0	10.7	3.7	6.4	5.4 ± 1.6	104	1.5	9.8
PSR J1057−5226	B1055−52	30.1	22.2	0.18	0.72	0.31 ± 0.1	99	0.8	15.5
PSR J1359−6038	B1356−60	293.7	24.0	0.30	0.93	0.43 ± 0.1	159	0.50	18.6
PSR J1400−6325†	–	563.0	28.5	0.32	1.00	0.48 ± 0.1	142	0.61	20.8
PSR J1453−6413	B1449−64	70.1	27.9	0.39	1.31	0.63 ± 0.2	134	0.61	27.2
PSR J1456−6843	B1451−68	8.6	24.8	0.58	1.8	0.93 ± 0.3	109	0.4	24.3
PSR J1534−5334	B1530−53	24.8	24.5	0.25	0.82	0.42 ± 0.1	117	0.75	15.1
PSR J1651−4246	B1648−42	482.0	18.2	0.48	1.70	1.08 ± 0.3	144	0.75	21.0
PSR J1707−4053	B1703−40	360.0	16.0	0.58	1.3	0.80 ± 0.2	84	0.45	14.1
PSR J1752−2806	B1749−28	50.4	20.0	0.67	1.84	1.17 ± 0.4	86	1.0	20.0
PSR J1820−0427	B1818−04	84.4	20.2	0.48	1.41	0.83 ± 0.2	134	0.81	16.6
PSR J1900−2600	B1857−26	38.0	24.0	0.21	0.73	0.37 ± 0.1	85	0.93	16.2
PSR J2048−1616	B2045−16	11.5	25.0	0.29	0.89	0.52 ± 0.1	132	0.93	18.5

images for our sample of 17 pulsars to produce complete light curves. For each detected pulsar location, we obtained all MWATS observations that were within a radius of 12°. These observations were then reduced and imaged as discussed above. We aimed to image pulsars within 12° of the pointing centre to reduce the effects of uncertain primary beam correction (discussed further below). This is also to mitigate against the drop-off in sensitivity towards the edge of the beam. Two of the pulsars (PSR J0034−0721 and PSR J1456−6843) were located greater than 12° from our pointing centre but we include them in this analysis. This is because they are bright with low DMs and as such we predicted that we might be able to detect variability.

3.2 Flux density scale correction

3.2.1 Relative flux scale

We calibrated the relative flux density scale of each snapshot image. This calibration consisted of comparing the flux density of unresolved sources detected within each image, to the flux density of sources from the SUMSS or VLSS catalogues. The SUMSS catalogue was used for images south of −30° declination, whilst the VLSS was used for sources north of this declination. For each snapshot image, we calculate the mean ratio of the MWA sources to that expected from either of the reference catalogues. Since the SUMSS, VLSS, and MWATS surveys are all at different frequencies (843, 74, and 154 MHz, respectively), we scaled the reference catalogue flux densities to the MWATS frequency using a spectral index of $\alpha = -0.8$ (Lane et al. 2014). The mean flux density ratio f_g was then used to correct all the MWATS flux densities to be in line with the SUMSS or VLSS flux densities.

This method bootstraps the flux density scale of an ensemble of unresolved sources (in the MWA images) rather than from a single source, and ensures an internally consistent flux scale. Typically between 150–500, crossmatched sources are used for this calculation. For sources that are not expected to be variable, we see an epoch-to-epoch flux density variation of 2–5 per cent (calculated using approximately 1000 sources per pulsar field). We take this to be the accuracy of our relative flux density calibration.

3.2.2 Absolute flux scale

The method described above achieves a good relative flux density scale between epochs; it does not, however, guarantee that the absolute flux density scale is well calibrated with respect to other radio catalogues. It is an area of active research to adequately constrain the low-frequency flux density scale in the Southern hemisphere (e.g. see Callingham et al. 2015, Hurley-Walker et al. 2014, and Wayth et al. 2015). Noting that the absolute flux density scale is uncertain, we find the relative flux density scale correction between images to be sufficient to achieve the goals of this work.

3.3 Light-curve extraction

The light curves of the pulsars were extracted using a forced fit algorithm implemented in the AEGEAN (version 1.9.5) source finding software package (Hancock et al. 2012).The right ascension and declination of each of the pulsars were fitted in the respective images to return the flux density values. The beam properties recorded in the image headers were used to constrain the Gaussian fit. We used the peak flux density reported by AEGEAN for all subsequent analyses. We also fitted two neighbouring unresolved sources that

had a signal-to-noise ratio of above eight. The modulation indexes of these neighbouring sources were used to ascertain errors on the flux stability of the instrument. This will be discussed further in Section 3.5.

Due to the small angular sizes of the pulsars, they should be unresolved at the MWA resolution. We visually inspected a region within a radius 5 arcmin surrounding the pulsar positions for bright extended Galactic plane emission. Pulsars embedded in these complex regions were removed from our final sample. Extended emission can cause complications in obtaining adequate and stable measurements of flux density.

3.4 Variability statistics

For each pulsar light curve, we calculated the reduced χ_r^2 statistic. We used the assumption that the light curve of a given pulsar was non-variable and the weighted mean of the flux density measurements was used as a model for the test. The reduced χ_r^2 statistic is defined as

$$\chi_r^2 = \frac{1}{n-1} \sum_{i=1}^{n} \frac{(S_i - \tilde{S})^2}{\sigma_i^2}, \tag{1}$$

where S_i is the ith flux density measurement with variance σ_i^2 and n is the total number of epochs. The weighted mean flux density, $\tilde{S}$, is defined as

$$\tilde{S} = \sum_{i=1}^{n} \left(\frac{S_i}{\sigma_i^2} \right) / \sum_{i=1}^{n} \left(\frac{1}{\sigma_i^2} \right). \tag{2}$$

We also calculate the modulation index which is defined as

$$M = 100 \times (\sigma/\overline{S}), \tag{3}$$

where σ is the standard deviation of the flux density measurements and $\overline{S}$ is the arithmetic mean (not the weighted mean).

3.5 Error analysis

The errors reported by AEGEAN give a good characterization of the error in fitting a Gaussian to a point source in a single image. There are a number of other sources of error in our flux density measurements as follows.

(i) Primary beam errors: the precise primary beam response of the MWA is difficult to model with increasing distance away from the pointing centre (Sutinjo et al. 2015). To reduce this effect, we limit our analysis to within 12° of the pointing centre where this error is estimated to be around 5 per cent (see Loi et al. 2015b). We apply this restriction to 15 of the pulsars in our sample. For two of the pulsars, PSR J0034−0721 and PSR J1400−6325, this was impractical and we allowed measurements within 15° of the pointing centre.

(ii) Flux density scale correction errors: the flux density scale correction discussed in Section 3.2 is not robust to problem images e.g. those containing bright diffuse Galactic emission in the side lobes. Images with extreme flux density scale corrections $0.1 < f_g < 1.9$ were removed from this analysis. Images requiring extreme flux density scale corrections were often of poor quality. The resulting light curves obtained from using those images typically contained excess non-physical variability, which was clearly correlated with the extreme flux density scale corrections.

The range of corrections (f_g) we accept represents the different calibrator models that we have used for phase calibration. Note, the initial flux density scale of these calibrators was never intended for

absolute flux calibration (hence the need for a robust flux density scale correction). One of the calibrators we used required flux scale corrections $f_g \sim 0.15$ to bring the images on to a common flux scale. This resulted in a skewing of the acceptable flux scale corrections we used in the final light-curves.

(iii) Ionospheric: excited geomagnetic conditions can distort the location of background radio sources (e.g. see Loi et al. 2015a) which can in turn affect the accuracy of the flux scale correction and source-fitting algorithms. For example, when a number of bright MWA sources were incorrectly crossmatched with SUMSS counterparts, causing incorrect flux scale correction factors (f_g) and thus flux scale errors. Observations taken during heightened ionospheric activity, which had large positional offsets were removed from this analysis. This accounted for approximately 1 per cent of the total data.

All of the effects described above are difficult to separate out into individual time and position dependent error terms. We therefore bootstrapped our errors from two neighbouring sources (to the given pulsar) of similar flux, under the assumption that they were non-variable. For two sources, we measured the averaged modulation index $\overline{M}$ and added this in quadrature with the AEGEAN Gaussian errors e_{fit}^2 and source flux density S_i as follows:

$$e_i = \sqrt{e_{\text{fit}}^2 + \left(S_i \times \overline{M} \right)^2}. \tag{4}$$

e_i is the adjusted error on an individual pulsar flux density measurement S_i. By bootstrapping the errors in this way, we set the minimum variability that we are capable of detecting to that of the neighbouring sources. These are the errors used in the variability statistics described in Section 3.4.

4 RESULTS

We consider a source to be statistically variable if $\chi_r^2 > 2.0$. We made a low cut on the minimum χ_r^2 used to define variability as we have been conservative with our error propagation. Of the 17 pulsars, four showed significant variability and we discuss these below. A summary of our results is given in Table 2 and pulsar light curves are shown in Figs 1, 2, and 3.

4.1 PSR J0953+0755 (B0950+08)

We detected significant variability in PSR J0953+0755, with a modulation index over all epochs of $M = 131.3$ per cent and a $\chi_r^2 = 182.1$ (see Fig. 1). On one of the nights of observing (2015-04-14), extreme variability was detected. For approximately one hour, the flux density of the pulsar increased and peaked at $S_{\text{max}} = 16.4$ Jy (see Table 2). PSR J0953+0755 (Pilkington et al. 1968) has a low DM of 2.95 cm^{-3} pc and spin period of 0.25 s (Hobbs et al. 2004). This pulsar is known to scintillate at low frequencies, for example, Phillips & Clegg (1992) report observations consistent with diffractive scintillation.

Due to the high-signal-to-noise ratio of the pulsar detection during this time, we were able to examine the frequency structure of the variability in the image plane. We took the data from the night of 2015-04-14 and for each observation we imaged the data in 30×0.97 MHz sub-bands. For each of the sub-bands in each of the time slots, we used the AEGEAN forced fit algorithm (discussed above) to fit the flux density at the location of the pulsar. The dynamic spectrum resulting from these measurements is plotted in Fig. 4. We note that our observations are not continuous i.e. each of the snapshot observations integrate for 112 s and then return 4 min later

to that declination. Fig. 4 shows four distinct events with discrete time and frequency structure. The peak of the variability seen in some of the sub-bands was even higher than in the full-bandwidth data: a peak flux density of 48.6 Jy was observed at 142 MHz.

The modulation index in both frequency and time for all measurements in Fig. 4 (left) gives 85.6 per cent. As discussed in Narayan (1992), we may expect a modulation index of up to 100 per cent for diffractive strong scintillation. In some of the frequency and times bins shown in Fig. 4 the pulsar is undetected. The result of these non-detections would be to decrease the modulation index as the flux density measurements are only upper limits.

We followed the method described in Cordes (1986) to calculate a scintillation bandwidth and time-scale based on our observations. We calculated the 2D autocorrelation function of the dynamic spectrum which is shown in Fig. 4 (bottom row). To parametrize the autocorrelation function, we fitted a 1D Gaussian in the time and frequency axes, respectively. We followed the definition in Cordes (1986), whereby the half-width half-maximum in the frequency direction defines the scintillation bandwidth. We used the half width at the $1/e$ point to calculate the scintillation time-scale. From this analysis, we find a scintillation bandwidth of $\Delta\nu_d = 4.1$ MHz and a scintillation time-scale of $\Delta\tau_d = 28.8$ min. We note that due to our broad bandwidth (30 MHz), we expect approximately a factor of 3 difference in scintillation bandwidth between the top and the bottom of our band. For all the calculations above, we use the central frequency for all scalings.

We scaled the scintillation bandwidth and time-scale reported by Phillips & Clegg (1992) under the assumption that $\Delta\nu_d \propto \nu^{4.4}$ and $\Delta\tau_d \propto \nu^{1.2}$ (Cordes 1986). We find that at 154 MHz, the predicted scintillation time-scale is 21.6 min and the scintillation bandwidth is 4.5 MHz. The predicted scintillation time-scale is slightly shorter than our result of 28.8 min. The predicted and measured scintillation bandwidths are in good agreement. The amplitude of variability is extreme, but such cases have been reported before e.g. Galama et al. (1997).

We can calculate the expected time-scale for refractive scintillation (τ_r) using the scintillation bandwidth ($\Delta\tau_d$) and time-scale ($\Delta\nu_d$) via the following expression from Stinebring & Condon (1990):

$$\tau_r = \frac{4}{\pi} \left(\frac{\nu \Delta\tau_d}{\Delta\nu_d} \right) \propto \nu^{-11/5}. \tag{5}$$

Using our diffractive scintillation parameters, we find $\tau_r = 20.9$ h at 154 MHz. This is consistent with Gupta et al. (1993) who measure a refractive time-scale for this pulsar of 3.4 d at 74 MHz (also see Cole, Hesse & Page 1970). There also appears to be a time-scale of several hundred days in the Gupta et al. (1993) data, the origin of which is unclear but could be inhomogeneties in the ISM.

This pulsar was recently observed with the LWA at 39.4 MHz and a number of giant pulses were detected that had a signal-to-noise ratio greater than 10 times that of the mean pulses (Tsai et al. 2015). These giant pulses were however typically reported to be rare with approximately 5 per hour (or 0.035 per cent of the total number of pulse periods). Singal & Vats (2012) observed this pulsar at 103 MHz with only 1.6 MHz of bandwidth. Scaling our results to their frequency, the scintillation bandwidth should be 0.7 MHz and the scintillation time-scale should be 18 min. At certain epochs, Singal & Vats (2012) report very strong pulses over the course of 30 min. Although they interpret this as giant pulse emission, we consider it much more likely to be the effects of scintillation. Giant pulses are largely broad-band in nature (Tsai et al. 2016), yet we see significant frequency structure in our observations. We therefore
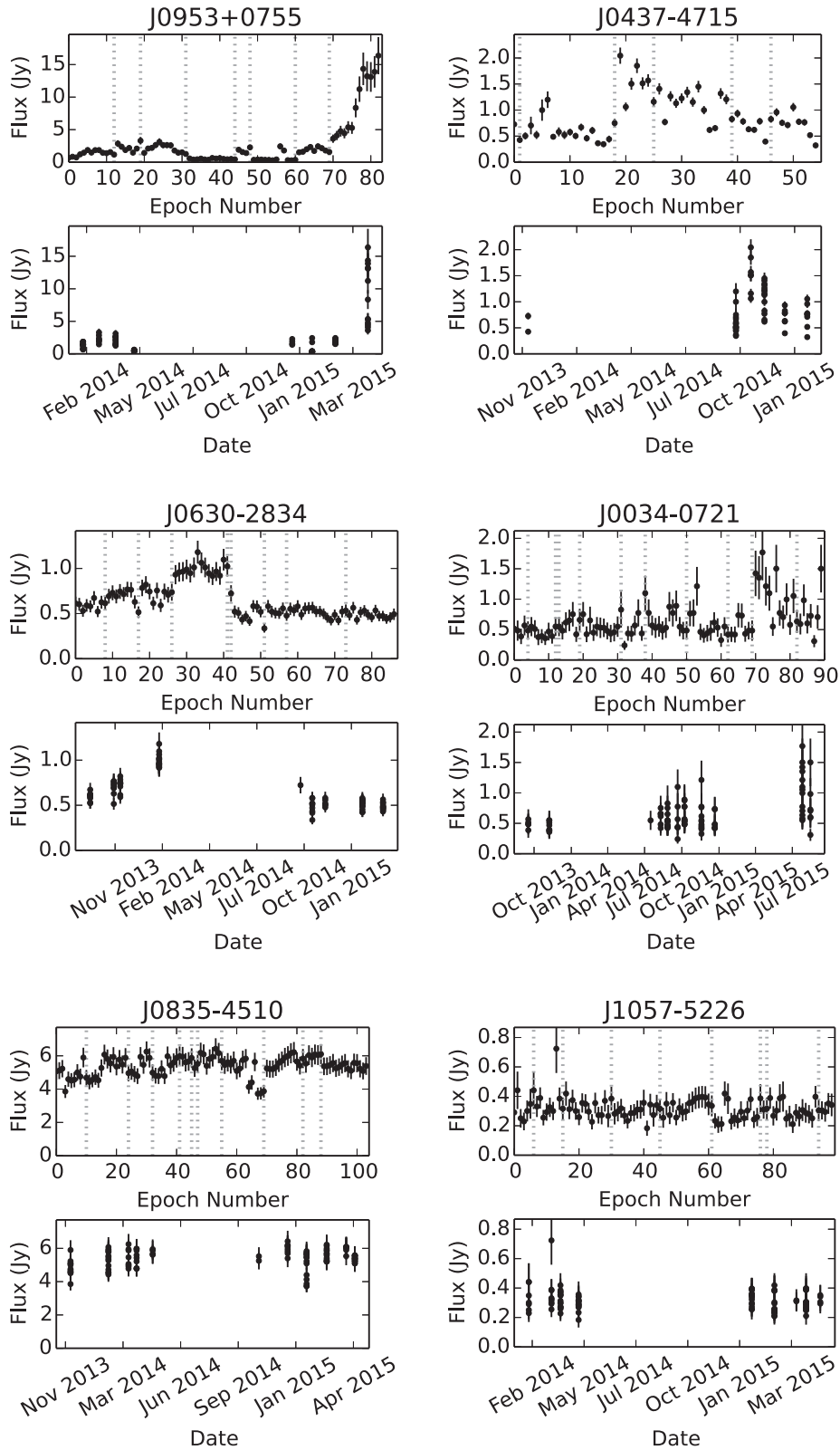
Figure 1. Light curves for nine pulsars detected at high-signal-to-noise ratio with the MWA. The top panel of each sub-plot shows the flux density as a function of sequential epoch number. The bottom panel shows the flux density as a function of date. The dashed grey line denotes an epoch number at which the time difference to the previous observation was greater than 8 d.
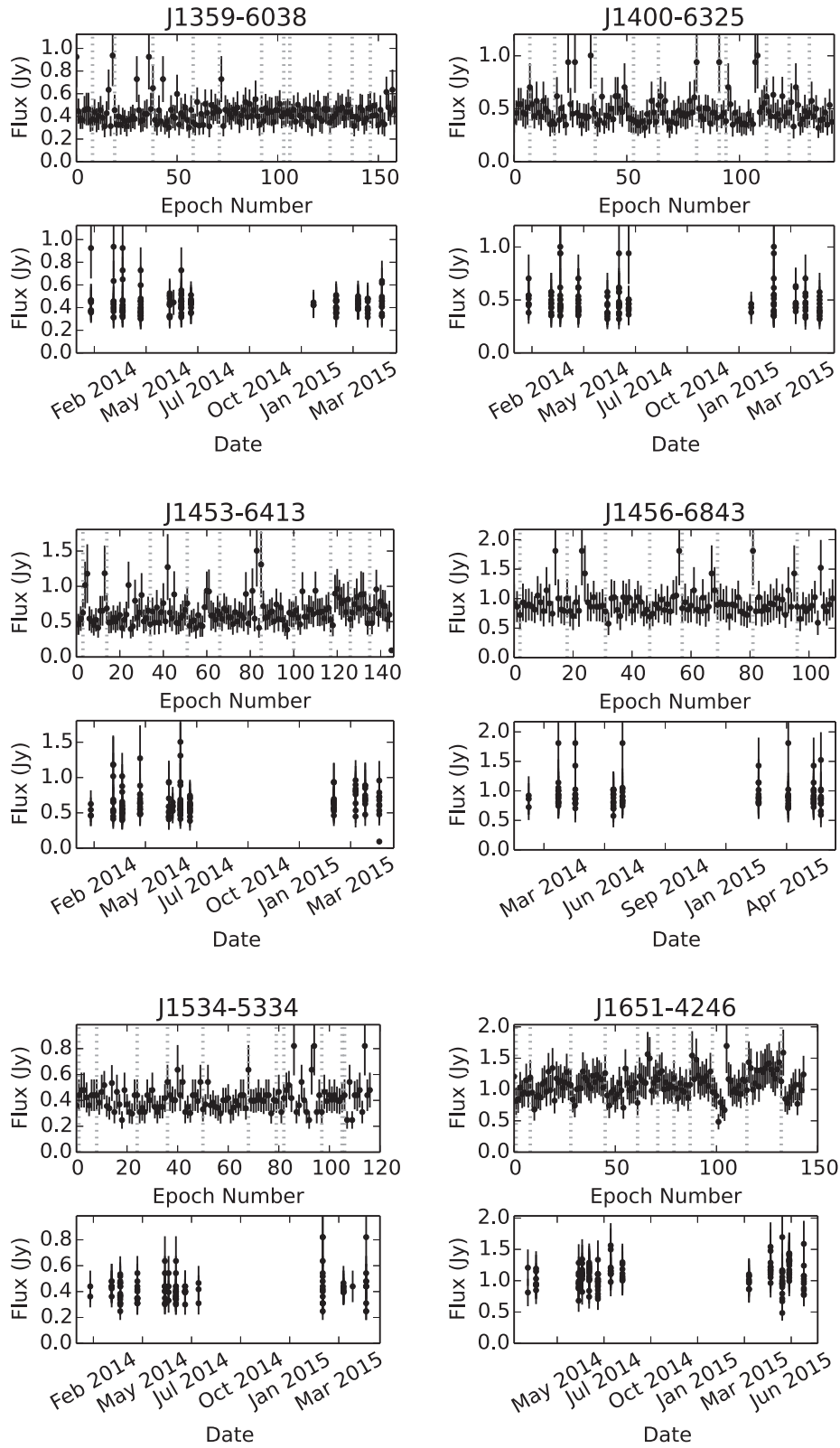
Figure 2. Light curves for eight pulsars detected at high-signal-to-noise ratio with the MWA. Details as in Fig. 1.
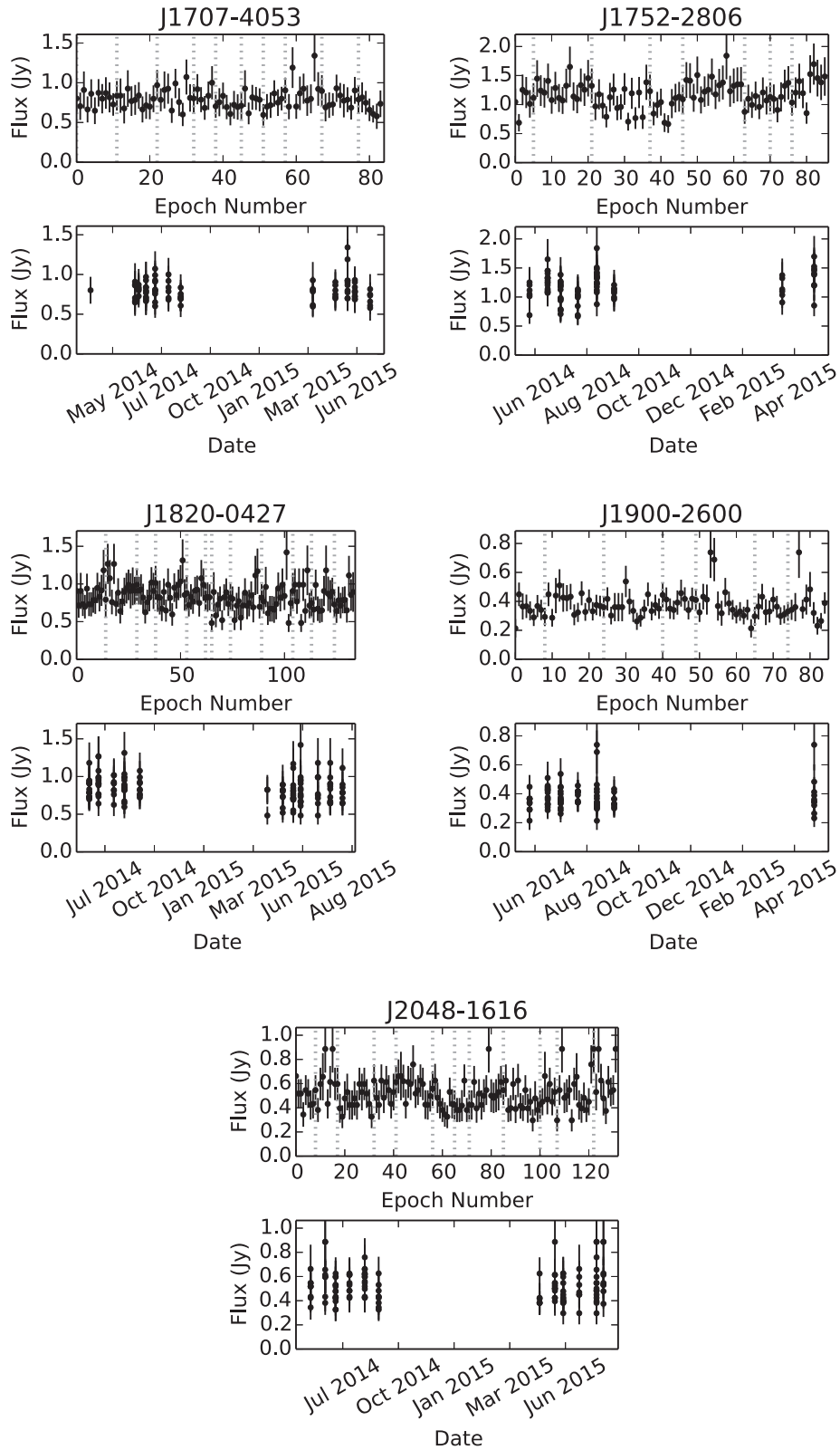
Figure 3. Light curves for eight pulsars detected at high-signal-to-noise ratio with the MWA. Details as in Fig. 1.
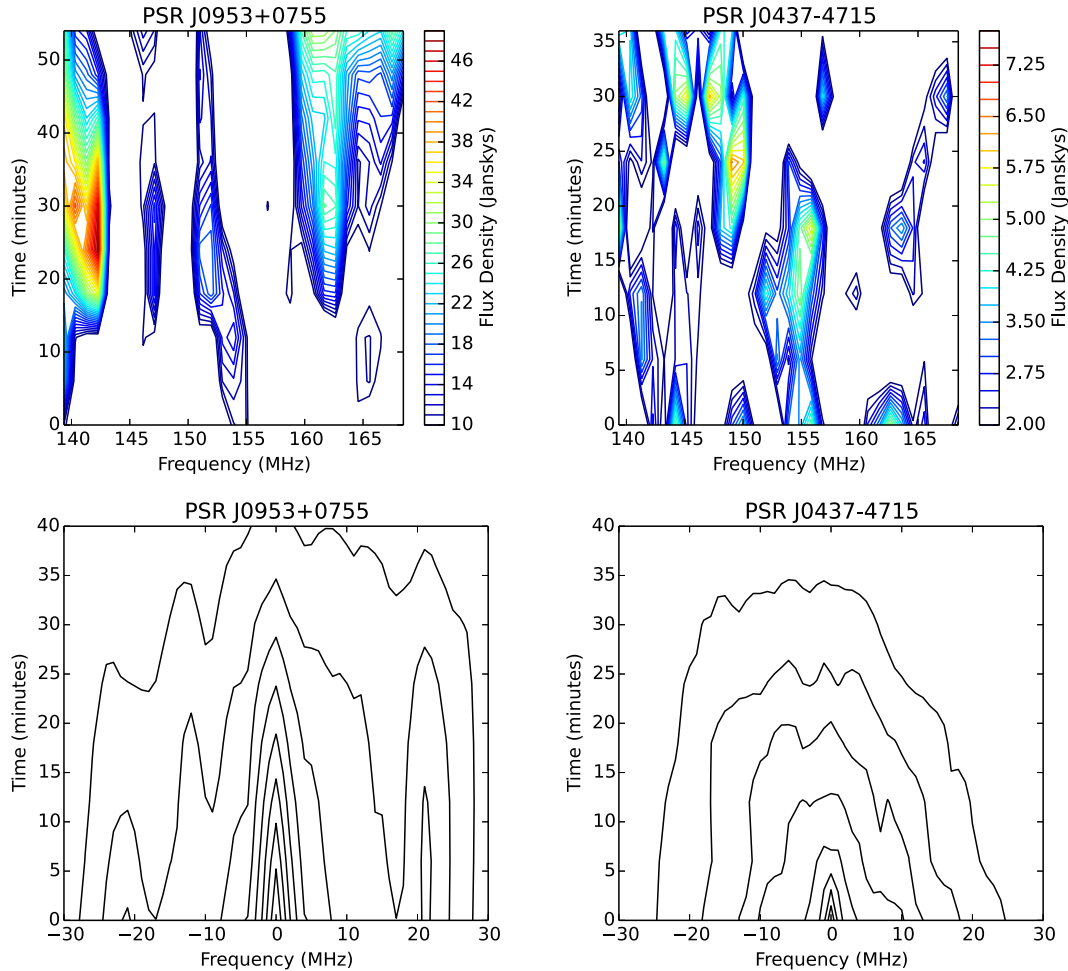
Figure 4. Top row: contour plots of the dynamic spectrum for the pulsars PSR J0953+0755 and PSR J0437−4715 during the most extreme levels of variability. The contours for these plots assume that the observations are continuous in time. For PSR J0953+0755, the contours run from 10 to 50 Jy in steps of 1 Jy; for PSR J0437-4715, they run from 2 to 8 Jy in steps of 0.25 Jy. Bottom row: 2D covariance functions of the dynamic spectra for the corresponding pulsars. 10 contour levels are shown that cover the peak to the minimum of the covariance function.

conclude that the extreme variability observed in PSR J0953+0755 is consistent with diffractive scintillation and is not intrinsic to the pulsar.

4.2 PSR J0437−4715

With a spin period of 5.76 ms and a DM of 2.65 cm^{-3} pc, PSR J0437-4715 is one of the closest and brightest millisecond pulsars (Johnston et al. 1993). This pulsar is located 7.3 deg away from the bright (452 Jy at 160 MHz; Slee 1995) double-lobed radio galaxy Pictor A, making this field challenging to image at low frequencies. The main issues arise when Pictor A is outside of the MWA field of view and is not de-convolved or CLEANed. This causes side-lobe flux to be scattered across the image, which in turn affects the image fidelity and the quality of the flux scale correction we are able to achieve and apply within that region. For the light curve shown in Fig. 1, we removed 14 observations that had extreme gain corrections and bad image fidelity.

We found a modulation index of $M = 44.9$ per cent with $\chi_r^2 = 28.1$. Bhat et al. (2014) have studied PSR J0437−4715 using the MWA at 192.6 MHz. For approximately one hour's worth of data with 20 s time resolution and 0.64 MHz of frequency resolution, the authors measure the scintillation properties. They report a scintil-

lation bandwidth of $\Delta\nu_d = 1.7$ MHz and a scintillation time-scale of $\Delta\tau_d = 4.5$ min. Using the frequency scaling $\Delta\nu_d \propto \nu^{3.9}$ and time scaling $\Delta\tau_d \propto \nu^{1.2}$ (see Bhat et al. 2014), these values become $\Delta\nu_d = 0.7$ MHz and $\Delta\tau_d = 3.5$ min at 154 MHz.

We repeated the same analysis described in Section 4.1 for the night of 2014-10-19, where the pulsar had the highest signal-to-noise ratio (a total of six observations). The dynamic spectrum is shown in Fig. 4 and this pulsar is clearly detected in the higher frequency resolution images with a flux density peaking around 7 Jy. The dynamic spectrum is much more discrete in frequency and time when compared with PSR J0953+0755. From the 2D autocorrelation analysis (see Fig. 4, bottom row), we find a scintillation bandwidth of $\Delta\nu_d = 3.1$ MHz and scintillation time-scale $\Delta\tau_d = 3.7$ min. The scintillation time-scale of 3.7 min from this study is in good agreement with the scaled value of 3.5 min from Bhat et al. (2014). The scintillation bandwidth of $\Delta\nu_d = 3.1$ MHz is however much broader than the scaled value of 0.7 MHz found by Bhat et al. (2014).

For this pulsar, we are only barely resolving the scintles in the frequency direction. Potentially, this broader value of $\Delta\nu_d$ is a result of this undersampling and uncertainties in obtaining a meaningful Gaussian fit to the autocorrelation function. We conclude that this variability is attributed to diffractive scintillation but note that our

scintillation measurements are at the lowest frequency to date, and greater frequency resolution would be beneficial in characterizing the scintillation further.

4.3 PSR J0630−2834 (B0628−28)

The pulsar PSR J0630−2834 (Large, Vaughan & Wielebinski [1969]) became brighter peaking at 1.2 Jy for one of the observing runs on 2013-12-06 (see Fig. [1]). The flux density then dropped to around 0.4 Jy in the observations six months later. We measure a modulation index of $M = 30.0$ per cent with a $\chi_r^2 = 5.8$. This pulsar is at a DM of 34.5 cm^{-3} pc (Hobbs et al. [2004]).

Scaling the scintillation bandwidth and time-scale reported by Cordes ([1986]), for this pulsar yields $\Delta\nu_d = 2.2$ kHz and $\Delta\tau_d = 1.2$ min. The predicted scintillation bandwidth (from Cordes [1986]) is almost three orders of magnitude less than our sub-band frequency resolution (0.97 MHz). We therefore conclude that the variability is not a consequence of diffractive scintillation.

Using equation (5), we find that the refractive scintillation time-scale is 74.2 d. The major jump in flux density corresponds to 239 d (about 7 months). The variability seen in this pulsar is more consistent with refractive scintillation with regards to time-scale. Averaging all the flux density measurements per night of observing and re-calculating the modulation index yields 24.0 per cent, which is slightly lower than the 30 per cent calculated from including all values independently. These values are consistent with the modulation that would be expected from refractive scintillation (see also Bhat, Rao & Gupta [1999a]).

4.4 PSR J0034−0721 (B0031−07)

PSR J0034−0721 was located at the edge of our survey region, so the only data available were where the pulsar was 9°–15° from the pointing centre of the observations. In this region, the primary beam correction is less accurate. A number of observations were also removed due to excited ionospheric conditions that affected source positions. The DM for this pulsar is 11.4 cm^{-3} pc (Hobbs et al. [2004]) and with the usable observations we detect mildly significant variability. We find a modulation index of $M = 45.0$ per cent with $\chi_r^2 = 2.0$. Scintillation bandwidth and time-scale values from Johnston, Nicastro & Koribalski ([1998]) scaled to 154 MHz are $\Delta\nu_d = 0.04$ MHz and $\Delta\tau_d > 8.7$ min.

The expected scintillation bandwidth is much smaller than our sub-band frequency resolution, therefore the variability is unlikely to be caused by diffractive scintillation. Using equation (5), we find a refractive time-scale of 30 d. The time difference between the final two epochs in Fig. [1], where the majority of the variability is concentrated, is 13 d. Averaging the flux density measurements per night of observing and calculating the modulation index yields 32.2 per cent, which is lower than for all measurements independently.

PSR J0034−0721 has been shown to undergo nulling (Huguenin, Taylor & Troland [1970]; Biggs [1992]). The nulls occur for a duration of up to 1 min and repeat pseudo-randomly every 100 pulses (Huguenin et al. [1970]). Noting that null duration is similar to the length of our observations (112 s), it is plausible that nulling could reduce the flux density significantly in a given observation. We conclude, however, that the cadence of the nulling (every 100 pulses, or every 94 s) would not cause the larger modulated, longer term variability seen in our observations (around epoch 70 onwards). Owing to the lower significance of variability ($\chi_r^2 = 2.0$) and difficult ionospheric conditions during observing, it is difficult to draw con-

clusions about the cause of variability for this pulsar, but refractive scintillation seems the most plausible.

4.5 PSR J0835−4510 (B0833−45)

We measure a modulation index of $M = 10.7$ per cent, which is very close to the average modulation index of two nearby sources $\overline{M} = 9.8$ per cent. This source had a $\chi_r^2 = 1.5$, meaning it is considered non-variable by our definition (see Section 4). We do however include it in this discussion as there are some noteworthy features.

PSR J0835−4510 is a pulsar with spin period 0.09 s and DM of 68.0 cm^{-3} pc. Historical low-frequency measurements of this pulsar by the Culgoora Circular Array (CCA; Slee [1995]) report flux densities of $S_{80} = 12$ Jy at 80 MHz and $S_{160} = 9$ Jy at 160 MHz with a spectral index of $\alpha = -0.42$. Here, we report a mean flux density of $S_{154} = 5.4 \pm 1.6$, which is significantly lower than the archival measurements. There is a distinct turnover in the spectrum (see Fig. [5]), which is potentially attributed to pulse broadening due to interstellar scattering (Higgins, Komesaroff & Slee [1971]).

Differences in flux density between our measurements and Slee ([1995]) could be attributed to instrumental differences. The CCA consisted of a circular 3 km baseline array and it lacked sensitivity to large, diffuse structure. With many short baselines, the MWA is sensitive to both diffuse and point-like emission. PSR J0835−4510 is embedded in a region of complex morphology, which includes both the pulsar and the Vela supernova remnant. We would therefore expect with its respective spatial sensitivity that the MWA would measure a greater flux density at the location of the pulsar, when compared with the CCA.

The size of the restoring beam was used to constrain the Gaussian fits to this object. This applies the assumption that this pulsar is represented by a single point source, which is unresolved. Separating the intrinsic flux of the pulsar from the contribution from the supernova remnant is difficult. We tested fitting this source with an unconstrained Gaussian and the reported major and minor axis of that fit were slightly larger than the restoring beam, indicating that this source is slightly resolved. Clearly, it is difficult within this region to obtain an accurate flux density via the method we have chosen.

This χ_r^2 is driven up by the apparent dip in the light curve around epoch 65, or 2015-01-20. So far, we have no explanation for a physical mechanism that would cause this dip but conclude that it is most likely a combination of source-fitting errors (discussed above) and difficulty in achieving adequate flux scale correction in such a complex region of the Galactic plane.

4.6 Non-variable pulsars

The remaining pulsars in our sample remained non-variable with $\chi_r^2 < 2.0$ and modulation indices comparable to the neighbouring sources. The non-variable pulsars are: PSR J1057−5226, PSR J1359−6038, PSR J1400−6325, PSR J1453−6413, PSR J1456−6843, PSR J1534−5334, PSR J1651−4246, PSR J1707−4053, PSR J1752−2806, PSR J1820−0427, PSR J1900−2600, and PSR J2048−1616. See Table [2] for full details of the statistics. See Figs [1], [2] and [3] for light curves.

Visual inspection of SUMSS images for the regions around PSR J1707−4053 and PSR J1400−6325 show low-levels of diffuse emission from supernova remnants. For this work, this emission is largely unresolved, but we note that a component of the flux density reported for these pulsars may originate from the supernova remnants.
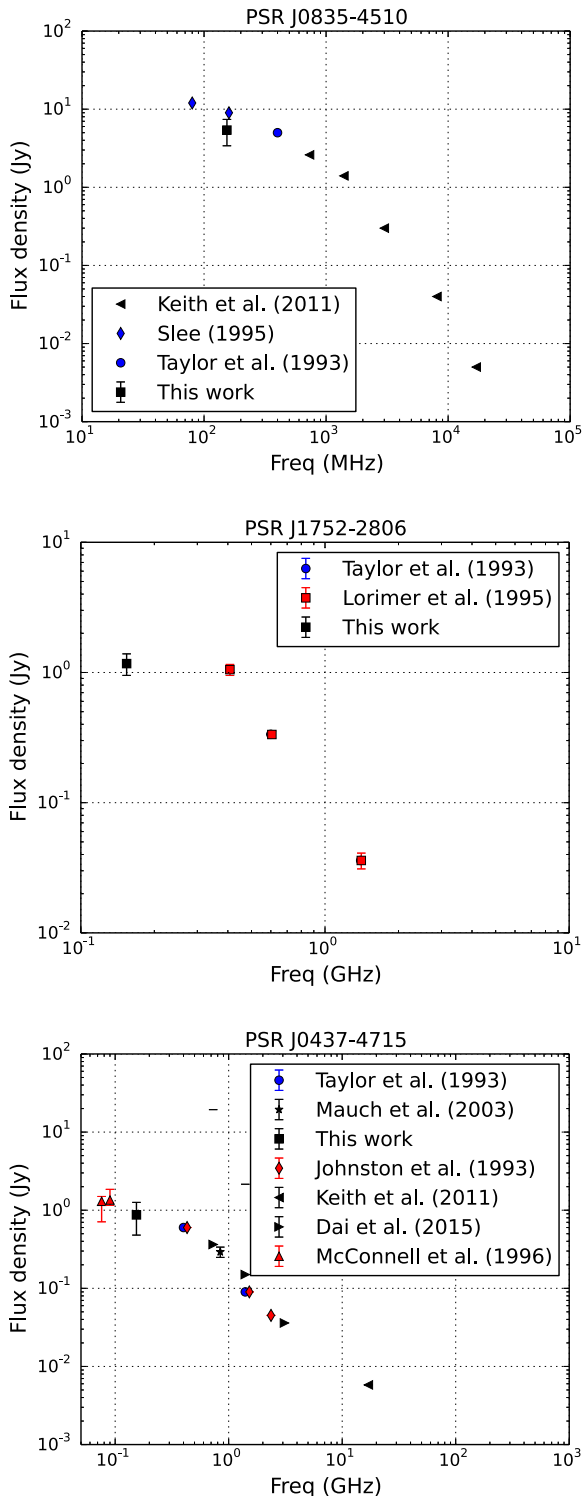
Figure 5. Spectral energy distributions of the pulsars PSR J0835−4510, PSR J1752−2806, and PSR J0437−4715. The archival data points are taken from Johnston et al. (1993), Taylor, Manchester & Lyne (1993), Lorimer et al. (1995), Slee (1995), McConnell et al. (1996), Mauch et al. (2003), Keith et al. (2011), and Dai et al. (2015).

4.7 Spectral properties of detected pulsars

We calculated a spectral energy distribution for each pulsar using an average flux density measurement for all data points from this work, and available data in the literature. A least-squares linear regression was used to find the spectral index and error (see Table 3). The pulsars PSR J1453−6413, PSR J1400−6325, and PSR J1534−5334 lacked sufficient archival data to calculate spectral indices.

In Fig. 5, we show spectra for the pulsars PSR J0835−4510, PSR J1752−2806, and PSR J0437−4715. These pulsars, especially PSR J1752−2806, show significant spectral curvature. We remind the reader of the discussion in Section 4.5 regarding the difficulties in obtaining an adequate flux density measurement for PSR J0835−4510. In Fig. 5 (left), our data point lies below archival measurements. In the case of PSR J1752−2806, even taking into account a 30 per cent uncertainty in our flux density scale, our data point is approximately an order of magnitude lower than what would be predicted based on the archival data points of Lorimer et al. (1995).

The mechanism for this curvature and possible turnover is currently uncertain. Previous studies claim that the abundance of pulsars with low-frequency turnovers is at most 10 per cent (Kijak et al. 2011; Bates, Lorimer & Verbiest 2013). Assuming three of the pulsars in our sample of 14 show spectral curvature, this equates to 21 per cent. This is supported by the recent work of Kuniyoshi et al. (2015), who show that in a sample of millisecond pulsars, 26 per cent display evidence for turnovers. Results from Bilous et al. (2015) also support this argument.

The average of our spectral index values for the pulsars is $\langle \alpha \rangle = -1.5 \pm 0.4$. A broad scatter is potentially a result of uncertainties in our absolute flux scale. This number is however in agreement with Bates et al. (2013) who report an average spectral index of $\langle \alpha \rangle = -1.41 \pm 0.96$, but slightly lower than Maron et al. (2000) who report $\langle \alpha \rangle = -1.8 \pm 0.2$. Our value is also in agreement with Bilous et al. (2015) who use low-frequency measurements and report $\langle \alpha \rangle = -1.4$. Bates et al. (2013) use population synthesis techniques and a likelihood analysis to model the underlying distribution, whereas Maron et al. (2000) derive their value empirically using measurements above 100 MHz only.

Calculating the mean spectral index of a population of pulsars is dependent on sufficient radio data spanning both MHz and GHz frequencies. It is compounded by frequency-dependent selection effects associated with such measurements. Including data below 100 MHz, where the spectral turnover is thought to most commonly occur, results in a flattening of the average spectral index (see Malofeev, Malov & Shchegoleva 2000; Bilous et al. 2015). The MWA has surveyed the Southern sky with frequency coverage between 72–231 MHz (see Wayth et al. 2015), and will contribute to exploring the low-frequency turnover of pulsar spectra further.

5 DISCUSSION

Fig. 6 shows the DM versus modulation index (left) and χ_r^2 versus modulation index (right) for this sample of pulsars. Four pulsars out of our sample of 17 show significant variability. For two of these pulsars (PSR J0953+0755 and PSR J0437−4715), we conclude that the variability is consistent with diffractive scintillation. A further two pulsars (PSR J0630−2834 and PSR J0034−0721) show variability that is best explained by refractive scintillation. This conclusion is less definitive for PSR J0034−0721.

Two of the pulsars, PSR J2048−1616 and PSR J1456−6843, show no significant variability despite their low DM

Table 3. Spectral indices of pulsars calculated using the average flux density from these observations plus arrival data. Dagger (†) denotes that the pulsar is poorly fit by a power law with significant spectral curvature. The spectral index distributions for these pulsars are shown in Fig. 5. The pulsar PSR J1057−5226 only had two measurements; therefore we do not report any errors. The references column lists the archival surveys used to calculate the spectral indices. The abbreviations indicate the first author of the survey and year of publication. The full references including the frequencies are in the table footnote.

Pulsar name	Spectral Index	References
PSR J0953+0755	−1.3 ± 0.1	L95, T93, S95, C98, D93, C07, M00
PSR J0437−4715†	−1.0 ± 0.1	J93, T93, M03, K11, D15
PSR J0630−2834	−1.6 ± 0.1	L95, T93, C98, D96, C07
PSR J0034−0721	−1.6 ± 0.2	T93, C98, M00
PSR J0835−4510†	−1.3 ± 0.2	T93
PSR J1057−5226	−0.95	T93
PSR J1359−6038	−1.9 ± 0.1	T93, N09, M78
PSR J1456−6843	−1.1 ± 0.1	T93
PSR J1651−4246	−2.1 ± 0.1	T93, M78
PSR J1707−4053	−2.1 ± 0.1	T93
PSR J1752−2806†	−1.7 ± 0.4	L95, T93
PSR J1820−0427	−2.1 ± 0.1	L95, T93
PSR J1900−2600	−1.5 ± 0.1	L95, T93, C98
PSR J2048−1616	−1.7 ± 0.2	L95, T93, N09, C98

M78 – Manchester et al. (1978) at 408 MHz; J93 – Johnston et al. (1993) at 430, 1520, and 2360 MHz; T93 – Taylor et al. (1993) at 400, 600, and 1400 MHz; L95 – Lorimer et al. (1995) at 408, 606, 925, and 1408 MHz; S95 – Slee (1995) at 160 MHz; D96 – Douglas et al. (1996) at 365 MHz; C98 – Condon et al. (1998) at 1400 MHz; M03 – Mauch et al. (2003) and Murphy et al. (2007) at 843 MHz, M00 – Malofeev et al. (2000) at 102.5 MHz, C07 – Cohen et al. (2007) at 74 MHz; N09 – Noutsos et al. (2008) at 1400 MHz, and Dai et al. (2015) at 730, 1400, and 3100 MHz.
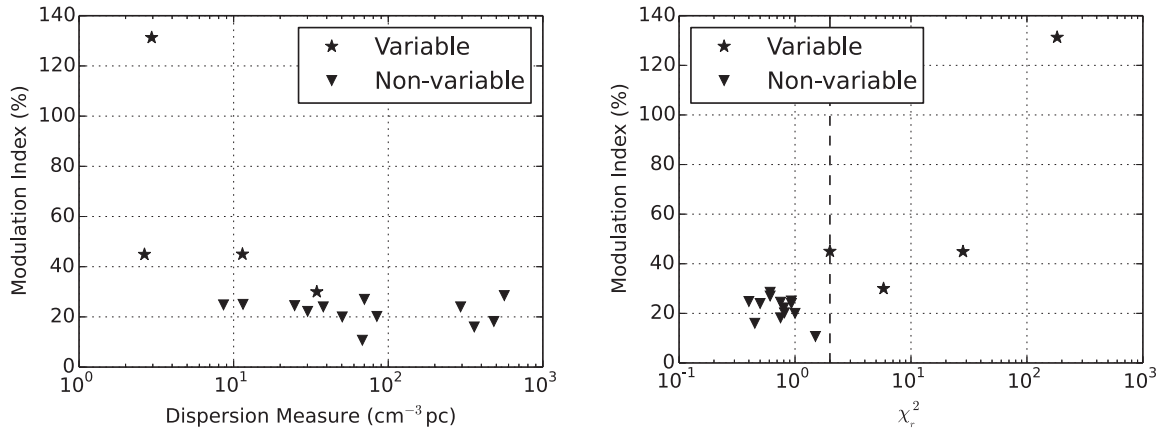

Figure 6. Left: plot of DM versus the modulation index for all pulsars in this sample. The pulsars shown with a starred symbol denote that significant variability was detected ($\chi_r^2 > 2$). Right: χ_r^2 versus modulation index. The dashed line shows $\chi_r^2 = 2$.

(DM <15 cm^{-3} pc). The lack of detection in these pulsars may be related to the probability of sampling bright diffractive scintillation events. This survey is limited by the conservative constraints we place on measurement errors. Reducing these uncertainties may indeed reveal significant variability for these pulsars in future analyses.

One question we would like to answer is whether we can make new detections of previously unknown pulsars blindly with this method using the MWA, or in the future with the Square Kilometre Array (SKA; Dewdney et al. 2009)? We have shown that MWATS can detect pulsars as transient sources through their scintillation properties. However, the bandwidth and time averaging that we perform implies that only those pulsars which have a scintillation bandwidth of at least a few MHz at 154 MHz are seen as transients. Using the Cordes & Lazio (2002) electron density model, we can infer a DM and hence distance we could probe with this limit on

the scintillation bandwidth. This yields a limit of 15.6 cm^{-3} pc or a distance of 0.6 kpc (assuming $l = 0$, $b = 0$). We also need to ensure that the pulsar is above the detection threshold of MWATS (100 mJy). In principle, therefore, we could detect a 10 mJy pulsar if the scintillation boost was a factor of 10 (similar to that seen for PSR J0953+0755). How many such pulsars exist in our Galaxy?

We simulate a pulsar population using PsrPopPy[2] (Bates et al. 2014), drawing spin periods and positions from distributions described by Lorimer et al. (2006) and luminosities from a lognormal distribution (Faucher-Giguère & Kaspi 2006). DMs were assigned by using the NE2001 model for the Galactic distribution of free electrons and the true distances to simulated sources. We populate the Galaxy with a population of ∼130 000 pulsars beaming along

[2] https://github.com/samb8s/PsrPopPy

our line of sight. Tallying only sources with DM$<$15.6 pc cm^{-3} and a flux density greater than 10 mJy, we find 125 ± 12 detectable pulsars in our simulations. The current pulsar catalogue contains some 50 pulsars which obey these criteria, thus there are of the order of 75 pulsars yet to be discovered that are within our survey parameters.

In principle we could probe a much larger volume of the Galaxy for pulsars if the data could be processed in 1 MHz channels rather than over the entire 32 MHz bandwidth. In this case, although the noise in each image would be higher, we would be sensitive to much narrower scintillation bandwidths corresponding to larger distances, increasing the likelihood of finding pulsars not currently detected by conventional searches.

6 CONCLUSION

With the MWA, we have detected significant variability in four pulsars using a sample of only 17 over almost the entire Southern hemisphere. One of the pulsars (PSR J0953+0755) shows extreme variability, of the order of a factor of 60. Both diffractive and refractive interstellar scintillation appear to explain the variability seen in our variable pulsar sample.

Signal to noise and good characterization of instrumental errors is required to generate adequate variability statistics. Improving upon our current techniques could offer further detections. Continued observations also harbour the possibility of detecting rare and bright events, such as that displayed in PSR J0953+0755. Future observations with an upgraded MWA with more tiles will allow for further exploration of the pulsar variability parameter space. This also includes refining the flux density measurements of the large number of low-signal-to-noise (3σ) ratio pulsars found via this work.

We predict that there are of the order of 75 pulsars that have not yet been detected via previous high time resolution surveys that could be detected by this method. These pulsars could potentially be of exotic or unusual type. Imaging observations with low-frequency wide-field interferometers therefore offer a new technique to explore and expand an already diverse population.

Prospects of exploring diffractive and refractive scintillation in imaging observations with the SKA are intriguing, especially exploring further DM ranges using the increased sensitivity and bandwidth capabilities. The possibility of detecting new pulsars via this imaging method is also promising. Assuming that a number of static continuum and time-domain surveys are completed with SKA, then we could contemplate these pulsar surveys being completed commensally. This is true for the data presented in this paper which has been the result of a broad science case blind transient survey (MWATS).

REFERENCES

Armstrong J. W., Rickett B. J., Spangler S. R., 1995, ApJ, 443, 209
Backer D. C., Kulkarni S. R., Heiles C., Davis M. M., Goss W. M., 1982, Nature, 300, 615
Bates S. D., Lorimer D. R., Verbiest J. P. W., 2013, MNRAS, 431, 1352
Bates S. D., Lorimer D. R., Rane A., Swiggum J., 2014, MNRAS, 439, 2893
Bhat N. D. R., Rao A. P., Gupta Y., 1999a, ApJS, 121, 483
Bhat N. D. R., Gupta Y., Rao A. P., 1999b, ApJ, 514, 249
Bhat N. D. R. et al., 2014, ApJ, 791, L32
Biggs J. D., 1992, ApJ, 394, 574
Bilous A. et al., 2015, preprint (arXiv:1511.01767)
Callingham J. R. et al., 2015, ApJ, 809, 168
Cohen A. S., Lane W. M., Cotton W. D., Kassim N. E., Lazio T. J. W., Perley R. A., Condon J. J., Erickson W. C., 2007, AJ, 134, 1245
Cole T. W., Hesse H. K., Page C. G., 1970, Nature, 225, 712
Condon J. J., Cotton W. D., Greisen E. W., Yin Q. F., Perley R. A., Taylor G. B., Broderick J. J., 1998, AJ, 115, 1693
Cordes J. M., 1986, ApJ, 311, 183
Cordes J. M., Lazio T. J. W., 2002, preprint (astro-ph/0207156)
Dai S. et al., 2015, MNRAS, 449, 3223
Deich W. T. S., Cordes J. M., Hankins T. H., Rankin J. M., 1986, ApJ, 300, 540
Dewdney P. E., Hall P. J., Schilizzi R. T., Lazio T. J. L. W., 2009, Proc. IEEE, 97, 1482
Douglas J. N., Bash F. N., Bozyan F. A., Torrence G. W., Wolfe C., 1996, AJ, 111, 1945
Ellingson S. W., Clarke T. E., Cohen A., Craig J., Kassim N. E., Pihlstrom Y., Rickard L. J., Taylor G. B., 2009, Proc. IEEE, 97, 1421
Faucher-Giguère C.-A., Kaspi V. M., 2006, ApJ, 643, 332
Galama T. J., de Bruyn A. G., van Paradijs J., Hanlon L., Bennett K., 1997, A&A, 325, 631
Goodman J., 1997, New Astron., 2, 449
Gupta Y., Rickett B. J., Coles W. A., 1993, ApJ, 403, 183
Hancock P. J., Murphy T., Gaensler B. M., Hopkins A., Curran J. R., 2012, MNRAS, 422, 1812
Higgins C. S., Komesaroff M. M., Slee O. B., 1971, ApJ, 9, 75
Hobbs G., Lyne A. G., Kramer M., Martin C. E., Jordan C., 2004, MNRAS, 353, 1311
Hobbs G. et al., 2016, MNRAS, 456, 3948
Huguenin G. R., Taylor J. H., Troland T. H., 1970, ApJ, 162, 727
Hurley-Walker N. et al., 2014, PASA, 31, e045
Johnston S. et al., 1993, Nature, 361, 613
Johnston S., Nicastro L., Koribalski B., 1998, MNRAS, 297, 10
Johnston S., van Straten W., Kramer M., Bailes M., 2001, ApJ, 549, L101
Kaplan D. L., Condon J. J., Arzoumanian Z., Cordes J. M., 1998, ApJS, 119, 75
Kaspi V. M., Stinebring D. R., 1992, ApJ, 392, 530
Keith M. J., Johnston S., Levin L., Bailes M., 2011, MNRAS, 416, 346
Kijak J., Lewandowski W., Maron O., Gupta Y., Jessner A., 2011, A&A, 531, A16
Kondratiev V. I. et al., 2016, A&A, 585, A128
Kramer M., Lyne A. G., O'Brien J. T., Jordan C. A., Lorimer D. R., 2006, Science, 312, 549
Kuniyoshi M., Verbiest J. P. W., Lee K. J., Adebahr B., Kramer M., Noutsos A., 2015, MNRAS, 453, 828
Lane W. M., Cotton W. D., van Velzen S., Clarke T. E., Kassim N. E., Helmboldt J. F., Lazio T. J. W., Cohen A. S., 2014, MNRAS, 440, 327
Large M. I., Vaughan A. E., Wielebinski R., 1969, Nature, 223, 1249

Lazio T. J. W., Cordes J. M., de Bruyn A. G., Macquart J.-P., 2004, New Astron. Rev., 48, 1439

Loi S. T. et al., 2015a, Geophys. Res. Lett., 42, 3707

Loi S. T. et al., 2015b, MNRAS, 453, 2731

Lonsdale C. J. et al., 2009, Proc. IEEE, 97, 1497

Lorimer D. R., Kramer M., 2012, Handbook of Pulsar Astronomy. Cambridge Univ. Press, Cambridge

Lorimer D. R., Yates J. A., Lyne A. G., Gould D. M., 1995, MNRAS, 273, 411

Lorimer D. R. et al., 2006, MNRAS, 372, 777

McConnell D., Ables J. G., Bailes M., Erickson W. C., 1996, MNRAS, 280, 331

Malofeev V. M., Malov O. I., Shchegoleva N. V., 2000, Astron. Rep., 44, 436

Manchester R. N., Lyne A. G., Taylor J. H., Durdin J. M., Large M. I., Little A. G., 1978, MNRAS, 185, 409

Maron O., Kijak J., Kramer M., Wielebinski R., 2000, A&AS, 147, 195

Mauch T., Murphy T., Buttery H. J., Curran J., Hunstead R. W., Piestrzynski B., Robertson J. G., Sadler E. M., 2003, MNRAS, 342, 1117

Murphy T., Mauch T., Green A., Hunstead R. W., Piestrzynska B., Kels A. P., Sztajer P., 2007, MNRAS, 382, 382

Narayan R., 1992, Phil. Trans. R. Soc. A, 341, 151

Noutsos A., Johnston S., Kramer M., Karastergiou A., 2008, MNRAS, 386, 1881

Offringa A. R., van de Gronde J. J., Roerdink J. B. T. M., 2012, A&A, 539, A95

Offringa A. R. et al., 2014, MNRAS, 444, 606

Offringa A. R. et al., 2015, PASA, 32, e008

Oronsaye S. I. et al., 2015, ApJ, 809, 51

Phillips J. A., Clegg A. W., 1992, Nature, 360, 137

Pilkington J. D. H., Hewish A., Bell S. J., Cole T. W., 1968, Nature, 218, 126

Rickett B. J., 1977, ARA&A, 15, 479

Sieber W., 1982, A&A, 113, 311

Singal A. K., Vats H. O., 2012, AJ, 144, 155

Slee O. B., 1995, Aust. J. Phys., 48, 143

Stappers B. W. et al., 2011, A&A, 530, A80

Stinebring D. R., Condon J. J., 1990, ApJ, 352, 207

Stinebring D. R., Smirnova T. V., Hankins T. H., Hovis J. S., Kaspi V. M., Kempner J. C., Myers E., Nice D. J., 2000, ApJ, 539, 300

Sutinjo A. T. et al., 2015, IEEE Trans. Antennas Propag., 63, 5433

Taylor J. H., Manchester R. N., Lyne A. G., 1993, ApJS, 88, 52

Tingay S. J. et al., 2013, PASA, 30, e007

Tsai J.-W. et al., 2015, AJ, 149, 65

Tsai -W., Jr, Simonetti J. H., Akukwe B., Bear B., Gough J. D., Shawhan P., Kavic M., 2016, AJ, 151, 28

van Haarlem M. P. et al., 2013, A&A, 556, A2

Wayth R. B. et al., 2015, PASA, 32, e025

Zhou A. Z., Wu X. J., Esamdin A., 2003, A&A, 403, 1059

This paper has been typeset from a TEX/LATEX file prepared by the author.